Antiferromagnetic ordering in Li_2MnO_3 single crystals with a two-dimensional honeycomb lattice

2012 J. Phys.: Condens. Matter 24 456004

(http://iopscience.iop.org/0953-8984/24/45/456004)

IOP PUBLISHING JOURNAL OF PHYSICS: CONDENSED MATTER

J. Phys.: Condens. Matter **24** (2012) 456004 (9pp) doi:10.1088/0953-8984/24/45/456004

Antiferromagnetic ordering in Li_2MnO_3 single crystals with a two-dimensional honeycomb lattice

Sanghyun Lee[1,2,3], Seongil Choi[1,2,3], Jiyeon Kim[2], Hasung Sim[1,2,4], Choongjae Won[5], Seongsu Lee[6], Shin Ae Kim[6], Namjung Hur[5] and Je-Geun Park[1,2,4]

[1] IBS Center for Functional Interfaces of Correlated Electron Systems, Seoul National University, Seoul 151-742, Korea
[2] Center for Strongly Correlated Materials Research, Seoul National University, Seoul 151-742, Korea
[3] Department of Physics, SungKyunKwan University, Suwon 440-746, Korea
[4] FPRD Department of Physics and Astronomy, Seoul National University, Seoul 151-742, Korea
[5] Department of Physics, Inha University, Incheon 402-751, Korea
[6] Neutron Science Division, Korea Atomic Energy Research Institute, Daejeon 305-353, Korea

E-mail: jgpark10@snu.ac.kr

Received 16 August 2012, in final form 19 September 2012
Published 23 October 2012
Online at stacks.iop.org/JPhysCM/24/456004

Abstract

Li_2MnO_3 consists of a layered Mn honeycomb lattice separated by a single layer of LiO_6 octahedra along the *c*-axis. By using single crystal Li_2MnO_3 samples, we have examined the physical properties and carried out both powder and single crystal neutron diffraction studies to determine that Mn moments order antiferromagnetically at $T_N = 36$ K with an ordered magnetic moment of 2.3 μ_B perpendicular to the *ab* plane. We have also discovered that about 35% of the full magnetic entropy is released in the supposedly simple paramagnetic phase, indicative of unusual spin dynamics at higher temperature.

(Some figures may appear in colour only in the online journal)

1. Introduction

Magnetic layered compounds with several distinct lattices have been an ideal playground in the search for unusual magnetic ground states [1]. Recently, there has been a growing interest in magnetic systems with a honeycomb lattice, for which several novel ground states have been proposed [2]. Honeycomb lattices *per se* cannot be magnetically frustrated with nearest neighbor interaction alone, but it was experimentally discovered that they can also have a nonmagnetic ground state in the presence of strong frustration due to the next nearest neighbor interactions, as observed in $Bi_3Mn_4O_{12}(NO_3)$ [3]. A more recent theoretical study found that interesting new physics emerges when a honeycomb lattice is occupied by magnetic ions having both localized and itinerant character [4]. Remarkably, this interplay between the superexchange interaction of localized character and double exchange interaction of itinerant character leads to several distinctive phases, such as ferromagnetic metal, Yafet–Kittel insulator, dimerized insulator, canted dimerized insulator, and quasi-antiferromagnetic metal. Moreover, adding quantum fluctuation to a honeycomb lattice was shown theoretically to stabilize a sought-after quantum spin liquid phase between a state of massless Dirac fermions and an antiferromagnetically ordered Mott insulator [5].

A_2TMO_3 with A = Na, Li and TM = transition metal elements has a unique layered structure with transition metal layers separated by a single A–O layer. Depending on the different transition elements and external variables such as temperature and pressure, it forms in one of several crystallographic structures: $R\bar{3}m$, $C2/c$, $C2/m$, or $P2_1/m$ [6–8]. By varying degrees, all these structures except $R\bar{3}m$ have a honeycomb lattice of transition metal elements.

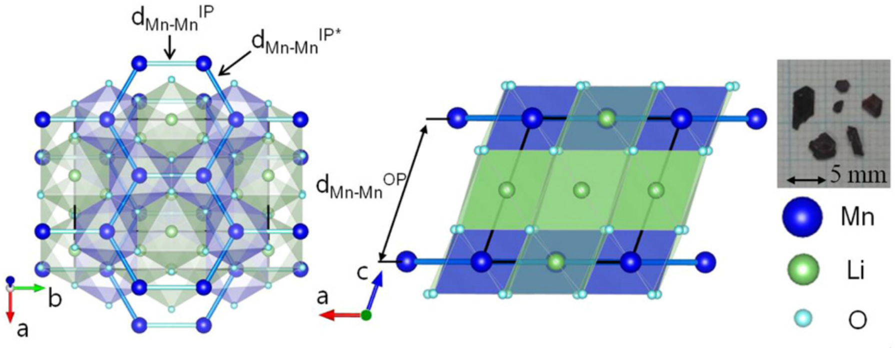

Figure 1. Li_2MnO_3 forms in the monoclinic $C2/m$ structure with Mn (Mn^{4+}, $S = 3/2$) ions having a honeycomb lattice. It is to be noted that because of the monoclinic structure with $\beta = 109.38°$, the c^* axis, not the c-axis, is perpendicular to the ab plane of the Mn honeycomb lattice. Different Mn–Mn bonds are marked too, and the photo shows typical single crystals used in this study. The thick line inside the structure indicates the unit cell.

Li_2TMO_3 is sometimes represented by another form of $Li(Li_{1/3}TM_{2/3})O_2$, similar to $LiCoO_2$, which is a well-known battery material in industry. $R\bar{3}m$ forms with disordered Li and TM in the $Li_{1/3}TM_{2/3}$ layer, while the other three structure forms with ordered Li and TM in the $Li_{1/3}TM_{2/3}$ layer. As far as TM honeycomb networks are concerned, $C2/m$ has only two different TM–TM bonds, while there are in principle three kinds of TM–TM bonds for $C2/c$ and $P2_1/m$. We will discuss the structure of $C2/m$ of Li_2MnO_3 in more detail shortly.

When the TM site is occupied by a 5d element like Ir with a strong intrinsic spin–orbit interaction, it was theoretically suggested that a quantum phase transition can be induced by about 2% of tensile strain for Na_2IrO_3 between a normal insulator and a topological insulator [9]. Because of the more extended character of Ir 5d bonds, spin density waves measurement by inelastic neutron scattering of Na_2IrO_3 found that there exists substantial exchange interaction beyond nearest neighbors, which then stabilizes a zig-zag magnetic order [7]. On the other hand, when the TM site is occupied by 4d elements such as Ru, with more localized electron bands and a strong spin–lattice coupling, a new magnetic state is found in Li_2RuO_3 with a concomitant metal–insulator transition at 540 K [8]. This magnetic phase was subsequently interpreted as a spin dimerized state via an orbital degeneracy [10].

Unlike the 4d and 5d transition elements, Mn having 3d electrons can be considered as a classical magnetic system with well localized moments. With 4+ valence, the three 3d electrons occupy all the low-lying t_{2g} levels of the Mn ion in the MnO_6 octahedra, which makes it Jahn–Teller inactive, i.e. no orbital degree of freedom left over. Like all the other honeycomb systems, it is also expected to have a small energy gap in the electronic density of states. Despite this rather apparent simplicity associated with the Mn system, nevertheless Li_2MnO_3 has a clear advantage over their 4d and 5d counterparts. Since it is a classical spin system one might be able to have a better control of its ground state by applying external variables such as pressure, magnetic fields and doping etc. We note that Li_2MnO_3 has been investigated as a candidate for electrodes in Li batteries in a form of composite material mixed with other Mn oxides [11].

In this paper, we report the complete physical properties of Li_2MnO_3 single crystals as well as neutron diffraction measurements using both powder and single crystal samples. According to our studies, Mn moments order antiferromagnetically below $T_N = 36$ K, with moments aligned perpendicular to the ab plane. Although most of its phase transition can be interpreted as an example of a classical system, it shows some signatures of unusual character too.

2. Experimental details

We have synthesized our powder samples by mixing Li_2CO_3 of 99.997% and MnO_2 of 99.99% in a stoichiometric ratio, which was then subjected to heat treatment at 1027 °C for 2 days. We added additional an 10% of Li_2CO_3 in order to compensate for the loss of Li. We note that heat treatment at a lower temperature such as 800–850 °C was reported to produce poor quality samples [12]. Thus we optimized our heat treatment condition in order to minimize Li loss through vaporization while, at the same time, achieving higher crystallinity of samples. We monitored the sample quality by measuring x-ray diffraction (XRD) patterns with a commercial diffractometer (MiniFlex II, Rigaku). Further higher resolution measurements and the temperature dependence of XRD patterns were obtained by using a commercial XRD (Empyrean, PANalytical) from 13 to 298 K with Cu $K\alpha_1$ $\lambda = 1.5406$ Å. Subsequent analysis confirmed that our powder sample forms in the $C2/m$ space group, as shown in figures 1 and 3. The summary of the crystal structure refinement is given in table 1 along with information on the atomic positions.

In order to grow single crystals, we mixed Li_2MnO_3 powder with Li_2CO_3 and B_2O_3 with a molar ratio of 1:2.76:2.39 inside a Pt crucible. The mixture was then heated to 1100 °C at a rate of 150 °C h^{-1} and kept there for 10 hrs before cooling back to 700 °C with a very slow cooling rate of 2 °C h^{-1}. Afterwards, the mixture was left for natural cooling to room temperature. Single crystals of black color obtained after water etching have typical dimensions of 2–5 mm long and 0.2 mm thick. A photo of a typical single crystal is shown as an inset in figure 1.

Table 1. Summary of crystal structure refinement results at 6 and 60 K.

HRPD at HANARO
Space group: $C2/m$ (No. 12)
$a \neq b \neq c, \alpha = \gamma = 90°$,
Mn(4g): $(0, y, 0)$, Li1(2b): $(0, 0.5, 0)$,
Li2(2c): $(0, 0, 0.5)$, Li3(4h): $(0, y, 0.5)$,
O1(4i): $(x, 0, z)$, O2(8i): (x, y, z)

	6 K	60 K
a (Å)	4.9166(1)	4.9167 (2)
b (Å)	8.5065(2)	8.5069(2)
c(Å)	5.0117(1)	5.0099(1)
β (deg)	109.376(2)	109.373 (2)
Volume (Å^3)	197.732(8)	197.678(9)
Mn y	0.1661(7)	0.1663(9)
Li3 y	0.6617(20)	0.6560(20)
O1 x	0.2190(8)	0.2178(9)
O1 z	0.2260(9)	0.2253(10)
O2 x	0.2533(5)	0.2537(6)
O2 y	0.3238(3)	0.3220(3)
O2 z	0.2231(5)	0.2237(6)
Mn B_{iso} (Å^2)	0.61(8)	0.73(9)
Li B_{iso} (Å^2)	0.93(10)	0.97(11)
O B_{iso} (Å^2)	0.60(3)	0.64(3)
$d^{\mathrm{IP}}_{\mathrm{Mn-Mn}}$ (Å)	2.826(8)	2.829(11)
$d^{\mathrm{IP}*}_{\mathrm{Mn-Mn}}$ (Å)	2.843(4)	2.841(5)
R_{p}	5.26	5.28
R_{wp}	6.80	6.84
R_{exp}	3.86	3.99
χ^2	3.11	2.93

We measured the magnetization of single crystal samples from 2 to 300 K by using a SQUID magnetometer (MPMS-5XL, Quantum Design) with a magnetic field of 30 Oe applied along and perpendicular to the *ab* plane. A further measurement was also carried out up to 700 K with a powder sample using a VSM magnetometer (Lakeshore VSM 735). Note that because of the monoclinic structure (β angle), as shown in figure 1, the crystallographic c-axis is not normal to the *ab* plane. Resistivity measurements were made between 283 and 400 K using a home-made setup for both in-plane and out-of-plane directions. We could not measure the resistance below 283 K because it becomes larger than 10^{12} Ω, too big even for our home-made high-resistance setup. We also employed a commercial system to measure heat capacity (PPMS-9T, Quantum Design) using a single crystal with a total weight of 4.33 mg.

In order to determine the magnetic structure, we carried out neutron diffraction experiments using both powder and single crystal samples. Our powder experiments were undertaken using a high-resolution powder diffractometer at HANARO reactor, Korea, from 6 to 60 K with a Ge(331) monochromator wavelength $\lambda = 1.8343$ Å for $2\theta = 10°$–$160°$. Single crystal neutron diffraction experiments were made using a four-circle diffractometer with a Ge(311) monochromator wavelength $\lambda = 1.3143$ Å using a sample of $4.5 \times 2.0 \times 0.2$ mm^3 at 10 K. For the single crystal experiments, we collected a total of 79 nuclear and 320 magnetic (*hkl*) Bragg peaks with the following conditions: $-5 \leq h \leq 0$, $-4 \leq k \leq 4$, and $-5 \leq l \leq 4$ for full Rietveld refinements. In order to check the temperature dependence of the magnetic order parameter, we also measured the temperature dependence of the two magnetic peaks of (−1 1 0.5) and (−1 −1 0.5) up to 60 K and four additional magnetic peaks of (0 −2 −1.5), (−1 −1 −0.5), (−1 −1 1.5), and (−2 2 1.5) and one more nuclear peak of (0 0 2) to 40 K. We employed Fullprof for Rietveld refinement [13].

3. Results and analysis

We measured the magnetic susceptibility of a Li_2MnO_3 single crystal using a small magnetic field of 30 Oe applied along and perpendicular to the *ab* plane. As shown in figure 2(a), our susceptibility shows a well-defined Curie–Weiss behavior above 100 K, with an effective moment of $\mu_{\mathrm{eff}} = 3.56$ and 3.43 μ_{B}/f.u. and a Curie–Weiss temperature of $\theta_{\mathrm{CW}} =$ 43 and 58 K for in-plane (χ_{IP}) and out-of-plane (χ_{OP}) susceptibility, respectively. We note that there is no anomaly in the susceptibility up to 700 K, above which Li evaporation begins to occur: we do not show the data above 300 K in figure 2 in order to keep the same temperature range in the figure as the other bulk data. Upon further cooling, a broad peak appears in the in-plane susceptibility at about 48 K, before getting increased again at lower temperature. On the other hand, the out-of-plane susceptibility develops a sharp drop below 36 K. This directional dependence of the magnetic susceptibility indicates that the magnetic easy axis is perpendicular to the *ab* plane.

As regards the transition temperature, it is worthwhile mentioning that in the literature there are two different magnetic ordering temperatures reported. One group associated a broad maximum with a magnetic ordering while the other group defined a sharp drop in susceptibility as an ordering temperature [14, 15]. In order to check which one of the two temperatures represents a true magnetic order, we performed heat capacity measurements using a single crystal sample with a total weight of 4.33 mg obtained from the same batch as the samples used for the susceptibility measurements. As shown in figure 2(b), our heat capacity show a clear peak at $T_{\mathrm{N}} =$ 36 K, where the susceptibility shows a big change in slope. It is interesting to note that when we took the temperature derivative of the out-of-plane susceptibility, $\mathrm{d}(\chi_{\mathrm{OP}}T)/\mathrm{d}T$, the resulting curve as shown in the inset of figure 2(a) resembles the temperature dependence of the magnetic heat capacity to be discussed shortly, in good agreement with a theoretical prediction [16]. This then lends support to our conclusion that the experimental heat capacity truly reflects the spin correlations measured by the susceptibility with $T_{\mathrm{N}} = 36$ K. In order to estimate the magnetic contribution of the heat capacity, we calculated the phonon contribution using a Debye model as shown below:

$$C_V = 9N_{\mathrm{Mn}}k_{\mathrm{B}}\left(\frac{T}{\theta_{\mathrm{Mn}}}\right)^3 \int_0^{\frac{\theta_{\mathrm{Mn}}}{T}} \mathrm{d}x \frac{x^4\mathrm{e}^x}{(\mathrm{e}^x-1)^2}$$

$$+ 9N_{\mathrm{Li,O}}k_{\mathrm{B}}\left(\frac{T}{\theta_{\mathrm{Li,O}}}\right)^3 \int_0^{\frac{\theta_{\mathrm{Li,O}}}{T}} \mathrm{d}x \frac{x^4\mathrm{e}^x}{(\mathrm{e}^x-1)^2},$$

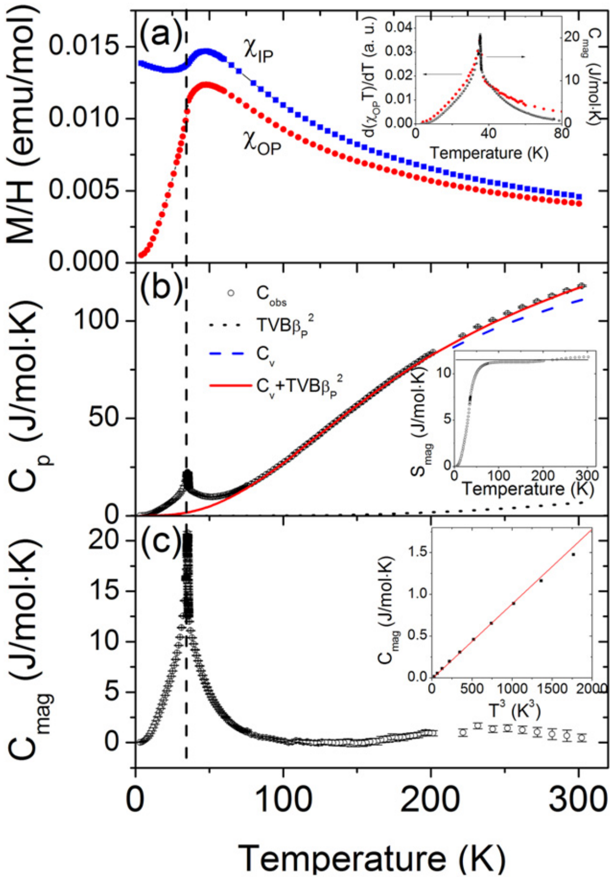

Figure 2. (a) Magnetization was measured using Li_2MnO_3 single crystals with 30 Oe applied along (χ_{IP}) and perpendicular (χ_{OP}) to the *ab* plane after zero field cooling. The inset displays the plot of $d(\chi_{OP}T)/dT$, which is in good agreement with the measured magnetic heat capacity, in accordance with the so-called Fisher's relationship [16], demonstrating that the measured heat capacity is mostly of magnetic origin. (b) Measured heat capacity (symbol) together with the phonon contribution estimated by using a Debye model (dashed line) with the Debye temperatures of $\theta_{Mn} = 444 \pm 9$ K and $\theta_{Li,O} = 822 \pm 3$ K. In order to explain the discrepancy at higher temperature between the data and the theoretical phonon contribution, we further calculated contributions of $TVB\beta_p^2$ (dotted line at the bottom of the figure) due to thermal expansion using the temperature dependence of x-ray data shown in figure 3. The combined total contribution is displayed as a solid line. (c) The resulting magnetic contribution of heat capacity is plotted with a peak at T_N. The inset presents the enlarged picture of the low-temperature part, displaying $C_{mag} \sim T^3$, indicative of a clear three-dimensional antiferromagnetic ordering.

where N is the number of atoms and θ is the Debye temperature. Because Li and O are far lighter elements than Mn, we used two different Debye temperatures for our calculations (dashed line): $\theta_{Li,O} = 822 \pm 3$ K and $\theta_{Mn} = 444 \pm 9$ K. As one can see, this theoretical phonon contribution appears to explain most of the temperature dependence up to 200 K, above which it begins to underestimate the measured data slightly. There might be a couple of reasons for this deviation, but after examining several possibilities we came to the conclusion that this deviation is most likely to be due to an isobaric volume expansion, namely a difference between the experimental isobaric heat capacity, C_p, and an isochoric heat capacity, C_v. This difference is expressed by $C_p–C_v = TVB\beta_p^2$, where B is a bulk modulus and β_p is an isobaric expansivity, which is usually small for most materials below room temperature since isobaric volume expansivity is negligible. However, as we have discovered below, it is not the case with Li_2MnO_3. This relatively large isobaric expansivity has certain implications in designing the electrodes of Li batteries using Li_2MnO_3, since this sizable expansivity is the source of a large strain being built up during thermal cycling [17].

In order to determine the isobaric expansivity experimentally, we examined the temperature dependence of XRD using powder Li_2MnO_3 samples. Some of the representative results are shown in figures 3(a) and (b) for the two temperatures at 298 and 13 K. Within the resolution of our XRD, there is no change in the crystal structure below and above the magnetic ordering. We note that the several well-resolved peaks in the range of $2\theta = 20°–30°$ indicate good crystallinity of Mn honeycomb layers, attesting the high quality of our sample. Our refinement results using Fullprof [13] are shown as the temperature dependence of the unit cell volume in figure 3(c). To fit the temperature dependence of the unit cell volume, we used the following Debye–Grüneisen formula:

$$V = V_{0,0}\left(1 + \frac{E(T)}{Q - bE(T)}\right), \qquad Q = \frac{V_{0,0}B_{0,0}}{\gamma},$$
$$b = \tfrac{1}{2}(B'_{0,0} - 1),$$

where $V_{0,0}$ is the unit cell volume at ambient pressure and base temperature, $B_{0,0}$ is a bulk modulus, $B'_{0,0}$ is the pressure derivative of the bulk modulus, γ is a so-called Grüneisen parameter and $E(T)$ is the total phonon energy at a given temperature. Since there is no experimental data for the bulk modulus of Li_2MnO_3 available, we instead used a value of MnO, $B = 144$ GPa, which has a similar rocksalt-type structure as Li_2MnO_3. We then fitted the data with the following set of parameters: $V_0 = 196.81$ Å^3, $\theta = 760$ K, $Q = 2.35 \times 10^{-17}$ J, and $b = 2.14$, similar to parameters successfully used for other materials [18, 19]. Note that the Debye temperature used here is very close to the numerical average of the two Debye temperatures used above for the analysis of the heat capacity. Using these parameters, we could obtain good fitting of the data, as shown in figure 3(c). From this temperature dependence, we calculated the isobaric expansivity, $\beta_p = 1/V(dV/dT)_p$ (see figure 3(d)). As a passing comment, the thus obtained result of the isobaric expansivity is very close to the reported volume expansivity of MnO and other rocksalt structures [20].

Using this experimentally determined isobaric expansivity, we have evaluated $C_p(= C_v + TVB\beta_p^2)$. As one can see in figure 2(c), this correction of $TVB\beta_p^2$ visibly improves the discrepancy seen at higher temperature in the previous attempt (dashed line). Since we have a fairly good estimate of the phonon contribution to the heat capacity in the paramagnetic phase, we are now able to deduce the magnetic contribution accurately, as shown in figure 2(c). We can further estimate the temperature dependence of the magnetic entropy (see the inset in figure 2(b)). Interestingly enough,

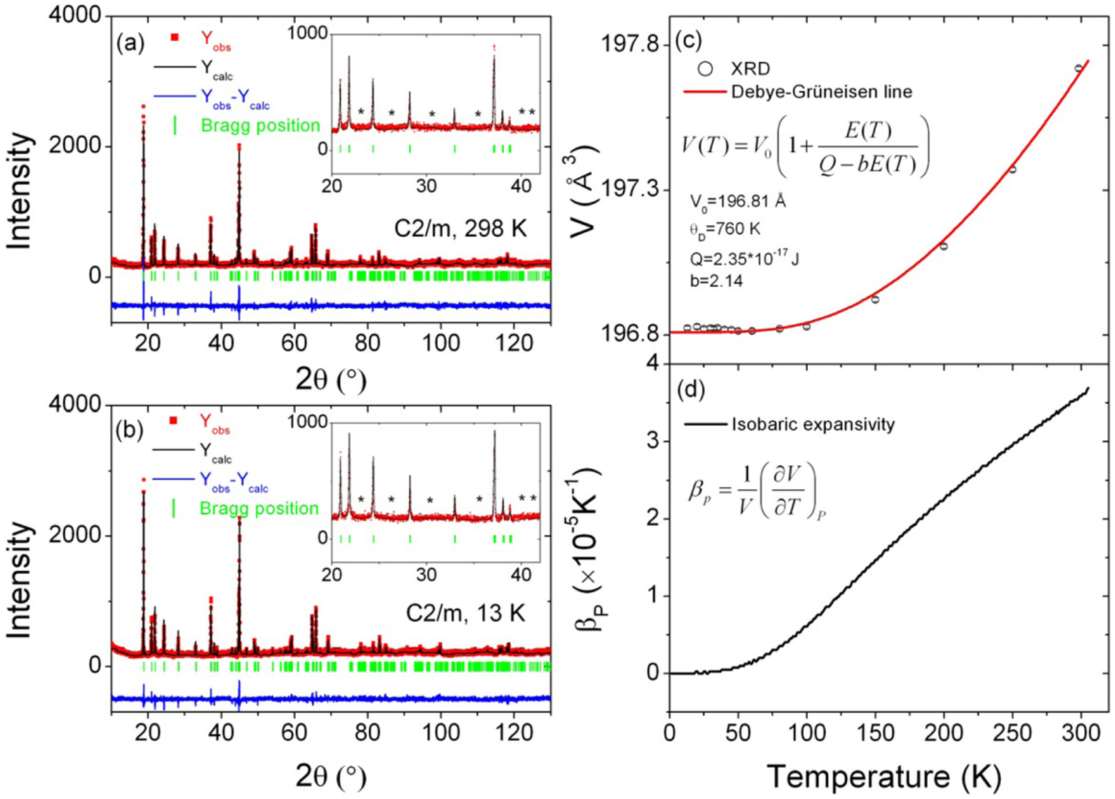

Figure 3. Two representative sets of XRD data taken at (a) 298 and (b) 13 K with symbols representing the measured data. Within the resolution of the XRD, all the Bragg peaks can be indexed according to the $C2/m$ space group. The bars just below the data points indicates the position of allowed nuclear Bragg peaks, the line through the data points are the refined results and the line at the bottom represents a difference curve between the measured data and the refined results. The insets show the blown-up picture of the low-angle data, with the position of superlattice peaks expected from the $C2/c$ space group marked by * symbols. (c) The measured unit cell volume (symbols) is shown together with the theoretical curve (line) obtained from the Debye–Grüneisen formula, as discussed in the text. From this theoretical curve, we then obtained the isobaric expansivity as shown in (d).

the magnetic heat capacity drops rather slowly above the transition temperature and even extends right up to $2T_N$, with about 35% of the total magnetic entropy being released above T_N. When integrated up to 150 K, then the total theoretical entropy is fully recovered with $S_{mag} = R\ln(2S+1) = 11.53$ J mol^{-1} K^{-1}, for $S = 3/2$ of Mn^{4+}. Usually this kind of large entropy released above T_N is seen in systems with strong frustration. However, we note that there is no clear evidence of the magnetic frustration in our measurements: for example, $f = |\theta_{CW}/T_N| = 1.6$. We acknowledge that the source of the magnetic entropy released above T_N is unexplained at the moment. The low-temperature behavior of the magnetic heat capacity shows a T^3 dependence, indicative of a three-dimensional antiferromagnetic ordering, as shown in the inset of figure 2(c).

In order to understand the electrical properties, we measured the in-plane (ρ_{IP}) and out-of-plane (ρ_{OP}) resistivity of Li_2MnO_3 as a function of temperature. As shown in figure 4, there is a very large anisotropy, of a factor of 10, in the two resistivity values: the out-of-plane resistivity is 8.6×10^{10} Ω cm at 300 K while the in-plane resistivity is 0.9×10^{10} Ω cm. This large anisotropic resistivity is quite conceivable considering the layered crystal structure of Li_2MnO_3. On the other hand, the gap energy estimated from the activation behavior is $\Delta \sim 0.72$ eV for the out-of-plane resistivity, whilst it is $\Delta \sim 0.61$ eV for the in-plane resistivity. This ratio of the two energy gaps is in good agreement with that of the anisotropic resistivity at room temperature.

We carried out both powder and single crystal neutron diffraction experiments in order to determine the magnetic structure. As clearly seen in the inset of figure 5(a), several magnetic superlattice peaks appear in the powder diffraction patterns upon cooling, which corresponds to a magnetic propagation vector of $Q_m = (0\ 0\ 0.5)$. Furthermore, when we examined the temperature dependence of the new magnetic superlattice peaks taken from the single crystal diffraction experiments they all follow the same temperature dependence below $T_N = 36$ K in the plot for the normalized F values in figure 5. While there is almost no visible change at T_N in the intensity of the (0 0 2) nuclear Bragg peak, as shown in figure 5(b). In principle, there are four possible magnetic structures with $Q_m = (0\ 0\ 0.5)$: Γ_{1g}, Γ_{2u}, Γ_{3g}, and Γ_{4u} (see figure 6 and table 2).

Among the four magnetic structures, one can immediately rule out both Γ_{1g} and Γ_{4u} based on the anisotropic susceptibility data shown in figure 2(a). It is also to be noted that the absence of the (0 0 1.5) magnetic superlattice peak (see the inset of figure 5(b)) disregards the Γ_{1g} model. Therefore, we are left only with the Γ_{2u} and Γ_{3g} magnetic

Table 2. Four possible representations for the $C2/m$ space group with the propagation vector of (0 0 0.5).

Mn(4g)	Γ_{1g}	Γ_{2u}	Γ_{3g}	Γ_{4u}
$(0\ y\ 0)$	$(0, S_y, 0)$	$(S_x, 0, S_z)$	$(S_x, 0, S_z)$	$(0, S_y, 0)$
$(0\ -y\ 0)$	$(0, S_y, 0)$	$(-S_x, 0, -S_z)$	$(S_x, 0, S_z)$	$(0, -S_y, 0)$
$(0.5\ 0.5+y\ 0)$	$(0, S_y, 0)$	$(S_x, 0, S_z)$	$(S_x, 0, S_z)$	$(0, S_y, 0)$
$(0.5\ 0.5-y\ 0)$	$(0, S_y, 0)$	$(-S_x, 0, -S_z)$	$(S_x, 0, S_z)$	$(0, -S_y, 0)$

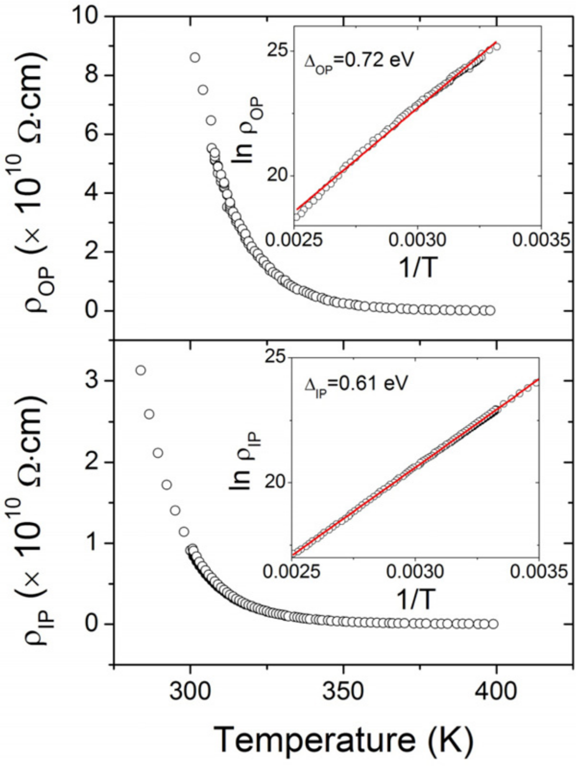

Figure 4. (Top) Out-of-plane (c^* direction) and (bottom) in-plane resistivity measured using a single crystal Li_2MnO_3 sample. Insets are plots of ln ρ versus $1/T$ and the lines represent simple activation behavior with an energy gap as shown in the figures.

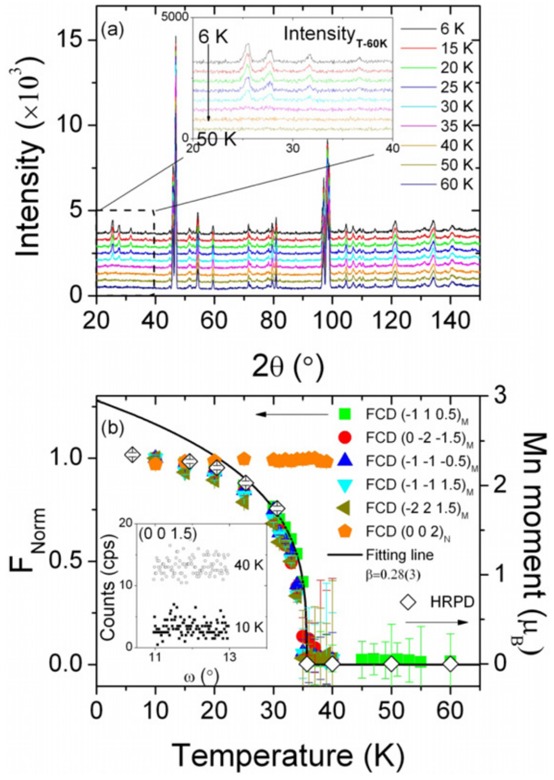

Figure 5. (a) Neutron powder diffraction patterns are shown from 6 to 60 K, with the inset displaying the temporal evolution of magnetic peaks at low angles after subtracting the data taken from the paramagnetic phase, i.e. at 60 K. (b) Temperature dependence of several magnetic peaks taken from single crystal neutron diffraction experiments (FCD) are shown as a function of temperature together with the temperature dependence of the magnetic moment (open diamond and denoted by HRPD) estimated from the refinement of the powder diffraction data as shown in (a). The line is for a theoretical curve of a mean-field type with $\beta = 0.28(3)$. The inset is added to show the absence of the (0 0 1.5) magnetic peak taken at below and above T_N with the 40 K data shifted upwards by 10 cps for the sake of presentation (see the main text).

structures. For the benefit of our discussion below, we would like to add comments on the Γ_{2u} and Γ_{3g} representations; the latter being the choice of a previous powder work [21]. The Γ_{2u} configuration has all Mn moment on the same honeycomb lattice ordering antiferromagnetically with antiferromagnetic coupling along the c axis. On the other hand, the Γ_{3g} configuration has all Mn moment on the same honeycomb lattice ordering ferromagnetically with antiferromagnetic coupling along the c axis. In particular, the authors of [21] proposed only the c-axis component, i.e. S_z, for the Γ_{3g} configuration.

The foregoing discussion notwithstanding, for reasons of rigor and completeness we present our full refinement results on both powder and single crystal diffraction data using the four possible magnetic models below. As one can see in figure 7, the best agreement as expected is only achieved with the Γ_{2u} model. Here we should point out the main difference between ours and that reported in [21]. While we came to a conclusion that the Γ_{2u} model is the correct magnetic structure the authors of [21] proposed the Γ_{3g} model with a c-axis component alone. However, it should be noted that if there is only an S_z component for the Γ_{3g} configuration one should expect the (0 0 1.5) peak to be nonzero because of the monoclinic crystal structure, in sharp contrast with the experimental data taken for a total counting time of 2 s (see the inset of figure 5(b)). For example, the expected counts of (0 0 1.5) based on the model of [21] is about 30 c s^{-1} (count per second) for the ordered moment of 3 μ_B while the background level was about 2–3 cps. Although the Γ_{3g} structure with moments perpendicular to the ab-plane cannot be ruled out, our Rietveld refinement disregards it based on the results shown in figure 7. A summary of the refinement results

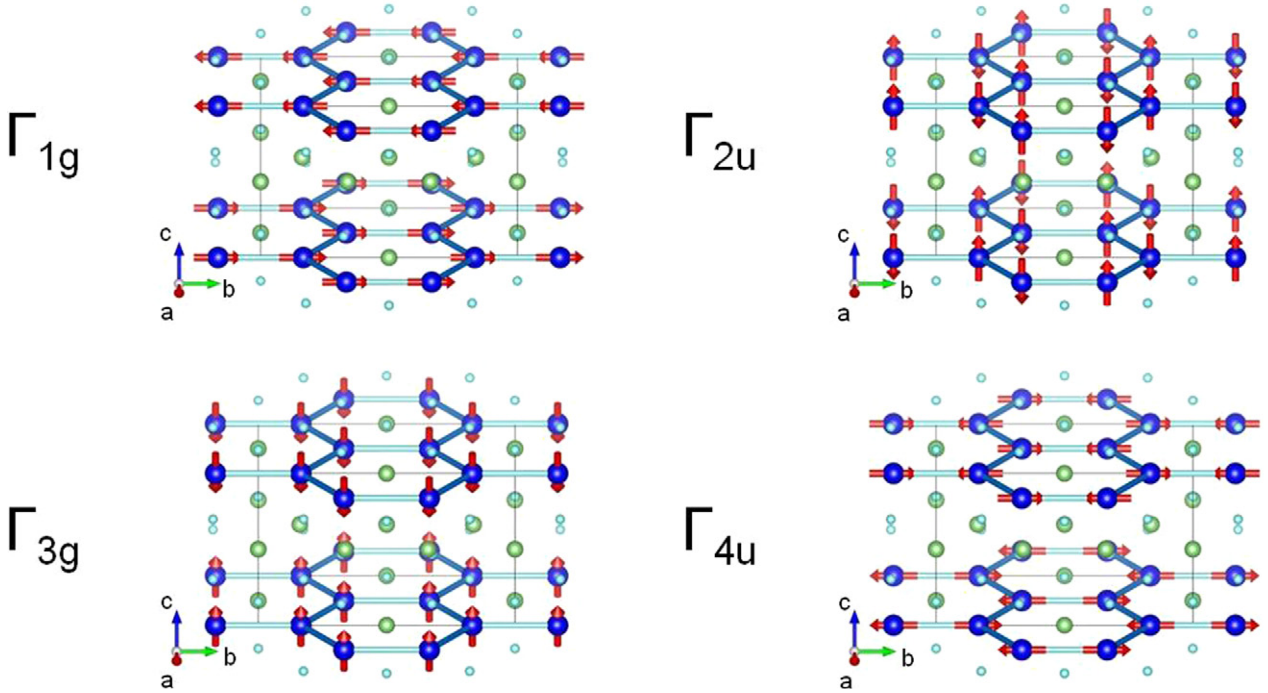

Figure 6. Four possible magnetic structures with $Q_m = (0\ 0\ 0.5)$ are shown with the unit cell displayed for each model.

Table 3. Summary of the magnetic structure refinement results for both powder diffraction data (HRPD) taken at 6 K and single crystal data (FCD) taken at 10 K using the Γ_{2u} model. Note that the total moment (M) smaller than its individual component (M_c in our case) arises simply from the monoclinic crystal structure. The angle θ_{spin} in the table is the angle of the moment with respect to the *ab* plane while the angle between the total moment and the *c*-axis of the monoclinic structure is 18.88°(HRPD) and 16.08°(FCD), respectively.

	HRPD		FCD
R_p	5.26	R_{F2}	22.1
R_{wp}	6.80	R_{WF2}	15.5
R_{exp}	3.86	R_F	40.3
χ^2	3.11	χ^2	2.20
M_a	0.803(69)	M_a	0.674(29)
M_b	0	M_b	0
M_c	2.486(24)	M_c	2.430(10)
M	2.3452(230)	M	2.2961(101)
θ_{spin}	90.5(2)	θ_{spin}	93.3(8)

is given in table 3. We think that the relatively large value of *R* factors is due to the mosaicity of the Ge monochromator of the FCD beamline.

A minor but nevertheless interesting issue is that although the expected moment of Mn^{4+} is 3 μ_B, assuming that the orbital moment is completely quenched as is often the case with half-filled t_{2g} levels, the obtained value of the ordered moment is only 2.3 μ_B, with about 0.7 μ_B missing and probably still fluctuating at low temperatures. We will discuss it with respect to another unusual aspect of the magnetism of Li_2MnO_3 later on.

Using the Γ_{2u} model, we continued to analyze all the other powder diffraction patterns taken at temperatures right up to 60 K, and plotted the temperature dependence of the magnetic moment in figure 5(b) together with the temperature dependence of a few magnetic superlattice peaks as obtained from the single crystal experiments. All these data, obtained from both powder and single crystal samples, clearly show that the magnetic phase transition occurs at $T_N = 36$ K, in which the out-of-plane magnetic susceptibility exhibits a marked change in slope. In addition, we have plotted a theoretical curve of a mean-field type for the ordered moment with $\beta = 0.28(3)$. We note that this value of β is somewhat off from a theoretical value $\beta = 0.325$ for a 3D Ising model, but interestingly our β value is similar to $\beta = 0.24(1)$ reported from a μSR experiment [14].

4. Discussion and summary

Li_2MnO_3 has a honeycomb network of Mn^{4+} moments and the three 3d electrons occupy the low-lying t_{2g} levels, which makes it Jahn–Teller inactive, i.e. no orbital degree of freedom at work. This configuration would then tend to make it a classic example of localized moments. Moreover, the honeycomb lattice is bipartite so *a priori* one would not expect to see any frustration unless these 3d electrons possess sufficient itinerant character giving rise to further nearest neighbor interactions. From this view point, several physical properties reported here on Li_2MnO_3 stand out and warrant further discussion. First and foremost, there is substantial magnetic entropy, about 35% of the total magnetic entropy of S_{mag}, being released above T_N. Then there is the relatively small size of the ordered moment as obtained from the neutron diffraction studies, which show that about 0.7 μ_B, i.e. 23% of the ionic moment, is still fluctuating at low temperatures. On the other hand, the so-called frustration

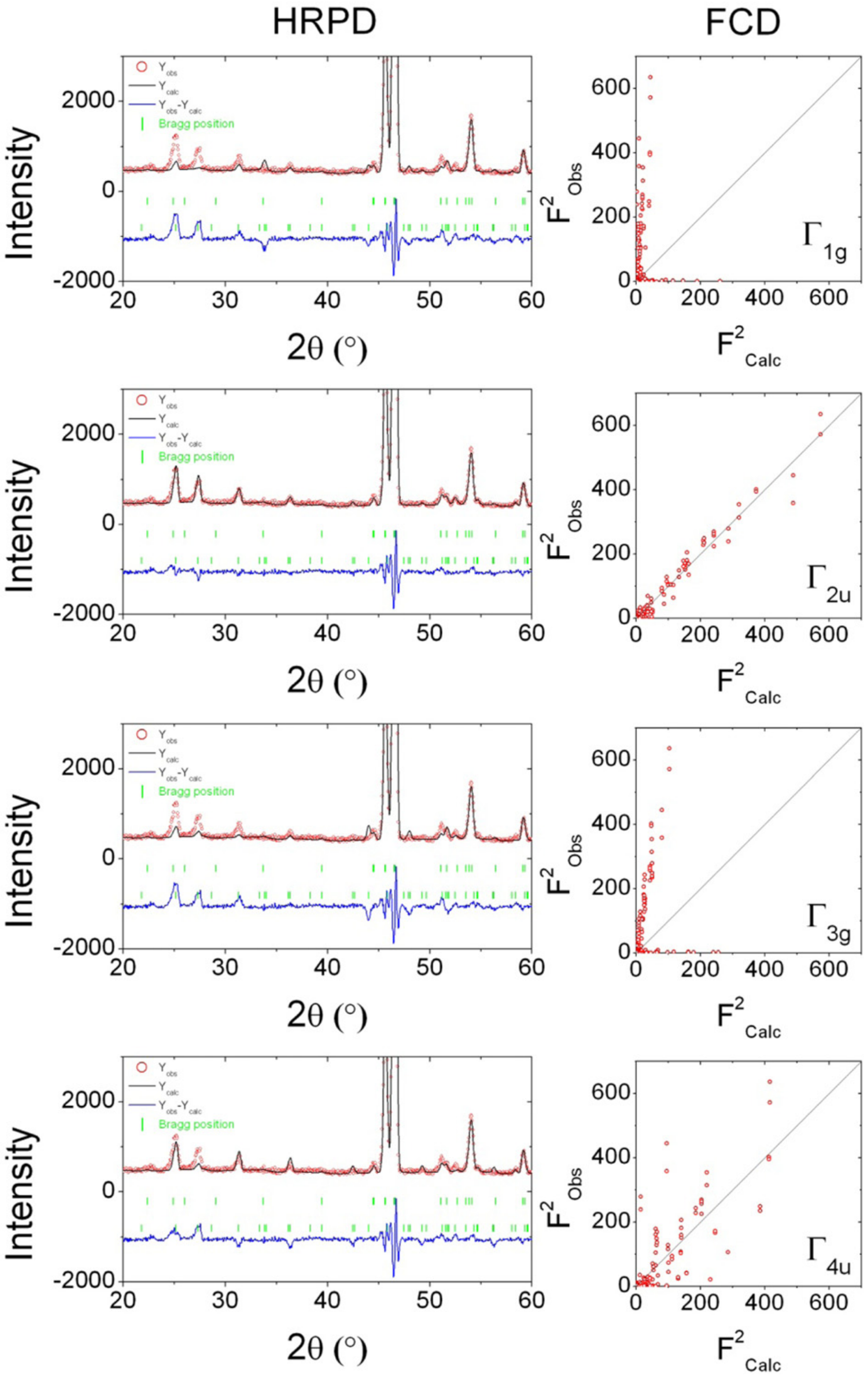

Figure 7. Final refinement results are shown of (left) powder neutron diffraction data (HRPD) taken at 6 K and (right) single crystal neutron diffraction data (FCD) taken at 10 K by using all possible four magnetic models: (from top to bottom) Γ_{1g}, Γ_{2u}, Γ_{3g}, and Γ_{4u}.

parameter defined as $f = |\theta_{CW}|/T_N$ is 1.6, barely larger than in any conventional magnetic systems. Furthermore, our neutron diffraction data shown in figure 5 failed to produce any evidence of diffuse scattering above T_N, unlike other systems with similar heat capacity behavior, which show strong diffuse scattering [22].

Of further interest is the magnetic ground state of the Γ_{2u} model, where all the neighboring Mn moments on the *ab* plane are antiferromagnetic ordered. The Mn–O–Mn bond angle on the plane is about 96°, which would favor ferromagnetic superexchange according to the Goodenough–Kanamori rule [23]. Thus one would expect to see a ferromagnetic configuration on the *ab* plane, in marked contrast with the observed antiferromagnetic ground state. This then indicates that there might exist some antiferromagnetic interaction in Li_2MnO_3 that is most likely to originate from *d*–*d* direct exchange interaction, as reported in other Mn compounds [24].

At this stage, it is interesting to compare the magnetic ordering of Li_2MnO_3 with that of $Bi_3Mn_4O_{12}(NO_3)$, which has the same Mn honeycomb lattice but does not order down to 0.4 K [3]. Theoretical studies using a density functional approach found that the ground state of $Bi_3Mn_4O_{12}(NO_3)$ is strongly frustrated due to long-range antiferromagnetic interactions [24], which is consistent with J values estimated from the inelastic neutron scattering [3]. A key difference between the two systems is that in the case of Li_2MnO_3 there is a Li atom at the center of the Mn honeycomb lattice, while it is unoccupied in $Bi_3Mn_4O_{12}(NO_3)$. Thus, it is interesting to ask whether there exist some magnetic exchange interactions through Li atoms for Li_2MnO_3. Another difference is that, while the Mn honeycomb lattice of Li_2MnO_3 is regularly separated by LiO_6 layers on both sides, it is sandwiched between a Bi layer and a NO_3 layer for $Bi_3Mn_4O_{12}(NO_3)$. This difference in the layered structure effectively makes the honeycomb lattice of $Bi_3Mn_4O_{12}(NO_3)$ a bilayer system. As a passing comment, the magnetic state induced by a magnetic field in $Bi_3Mn_4O_{12}(NO_3)$ is a Γ_{4u} representation among our four models shown in figure 6.

With this presence of possibly substantial direct exchange and the further interest of exchange interaction through Li atoms, it is an interesting question to ponder what would happen if one could control this exchange interaction by external means. For example, we estimate that external pressure in the range of 3 GPa, which is available at most modern high pressure labs, would produce about 2% of volume contraction if we use a bulk modulus value of $B = 144$ GPa for MnO. It can already be seen in some of the theoretical calculations for a magnetic honeycomb lattice that a pressure, or to be more specific a strain, of that range is strong enough to produce a new quantum phase transition in Na_2IrO_3 [9]. It would be interesting to see whether a similar amount of volume change could give rise to some significant change in the magnetic ground states for Li_2MnO_3. Moreover, another important question is to ask whether the expected increase of itinerant character of the exchange interaction will lead to a macroscopic degeneracy and emergent frustration, as predicted by a recent theoretical study [4]. It is possible that with even higher pressure a metallic phase might be stabilized, where one expects to see entirely different spin dynamics emerge.

To summarize, we have investigated Li_2MnO_3, a classic spin system of Mn^{4+} well localized magnetic moments with a honeycomb lattice. From this study, we have shown that it undergoes a simple collinear antiferromagnetic ordering below $T_N = 36$ K, where the ordered moment obtained from the neutron diffraction experiments starts to develop and there exists a clear peak in the experimental heat capacity. Furthermore, we have demonstrated that both the magnetic entropy estimated from the heat capacity data and the size of the ordered moment indicate that there might well be some kind of frustration at work, whose nature seems to be unclear at the moment. We also discussed some possible new phases that might emerge when subjected to external pressure.

Acknowledgments

We would like to acknowledge Junghwan Park, A Pirogov, A Wildes, Gun Sang Jeon, and Jaejun Yu for helpful discussions, and Inhwan Oh and Junki Hong for technical assistance. Work at Seoul National University was supported by the National Research Foundation of Korea (Grant Nos. KRF-2008-220-C00012 and R17-2008-033-01000-0). JGP was also supported by the Advanced Institutes of Convergence Technology: Grant #2010-P2-08.

References

[1] de Jongh L J *et al* 1990 *Magnetic Properties of Layered Transition Metal Compounds* (Dordrecht: Kluwer)
[2] Kitaev A 2006 *Ann. Phys.* **321** 2
[3] Matsuda M, Azuma M, Tokunaga M, Shimakawa Y and Kumada N 2010 *Phys. Rev. Lett.* **105** 187201
[4] Venderbos J W F, Daghofer M, van den Brink J and Kumar S 2011 *Phys. Rev. Lett.* **107** 076405
[5] Meng Z Y, Lang T C, Wessel S, Assaad F F and Muramatsu A 2010 *Nature* **464** 847
[6] Takahashi Y, Kijima N, Hayakawa H, Awaka J and Akimoto J 2008 *J. Phys. Chem. Solids* **69** 1518
Kataoka K, Takahashi Y, Kijima N, Nagai H, Akimoto J, Idemoto Y and Ohshima K 2009 *Mater. Res. Bull.* **44** 168
O'Malley M J, Verweij H and Woodward P M 2008 *J. Solid State Chem.* **181** 1803
[7] Choi S K *et al* 2012 *Phys. Rev. Lett.* **108** 127204
[8] Miura Y, Yasui Y, Sato M, Igawa N and Kakurai K 2007 *J. Phys. Soc. Japan* **76** 033705
[9] Kim C H, Kim H S, Jeong H, Jin H and Yu J 2012 *Phys. Rev. Lett.* **108** 106401
[10] Jackeli G and Khomskii D I 2008 *Phys. Rev. Lett.* **100** 147203
[11] Thackeray M M, Kang S-H, Johnson C S, Vaughey J T, Benedek R and Hackney S A 2007 *J. Mater. Chem.* **17** 3112
[12] Nakamura K, Hirano H, Michihiro Y and Moriga T 2010 *Solid State Ion.* **181** 1359
[13] Rodriguez-Carvajal J 1993 *Physica* B **192** 55
[14] Mukai K *et al* 2010 *J. Phys. Chem.* C **114** 11320–7
[15] Jansen M and Hoppe R 1973 *Z. Anorg. Allg. Chem.* **397** 279
Scharmann A, Vrrr B, Hoppe R and Meyer G 1975 *Phys. Status Solidi* b **72** 197
Felner I and Bradaric I M 2002 *Physica* B **311** 195
[16] Fisher M E 1962 *Phil. Mag.* **7** 1731
[17] Cho J, Kim Y J, Kim T-J and Park B 2001 *Angew. Chem.* **113** 3471
[18] Fortes A D, Wood I G, Brodholt J P, Alfredsson M, Vocadlo L, McGrady G S and Knight K S 2003 *J. Chem. Phys.* **119** 10806
[19] Lee S *et al* 2006 *Nature Mater.* **5** 471
[20] Smyth J R, Jacobsen S D and Hazen R M 2000 *Rev. Mineral. Geochem.* **41** 1
[21] Strobel P and Lambert-Andron B 1988 *J. Solid State Chem.* **75** 90
[22] Park J *et al* 2010 *Phys. Rev.* B **82** 054428
[23] Goodenough J B 1963 *Magnetism and the Chemical Bond* (New York: Interscience)
[24] Kandpal H C and van den Brink J 2011 *Phys. Rev.* B **83** 140412R